Top of document

SUPPLEMENTARY INFORMATION

Calcium-Dependent Hyperexcitability in Human Stem Cell-Derived Rett Syndrome Neuronal Networks

Pradeepan *et al.*

Table of Contents

Top of document

1 Supplementary Results

1.1 Bursting phenotypes in *MECP2* mutant neuronal networks

MECP2 mutant and control networks developed spontaneous activity, first appearing as sparse firing two weeks post-plating (Figure S1A, B). By week 3, networks began synchronously bursting – forming network bursts. Network bursts first formed with a high degree of inter-burst spikes that 'migrated' into bursts over development (Figure SR1). Strong synchronous bursting activity persisted until the end of the recording period.

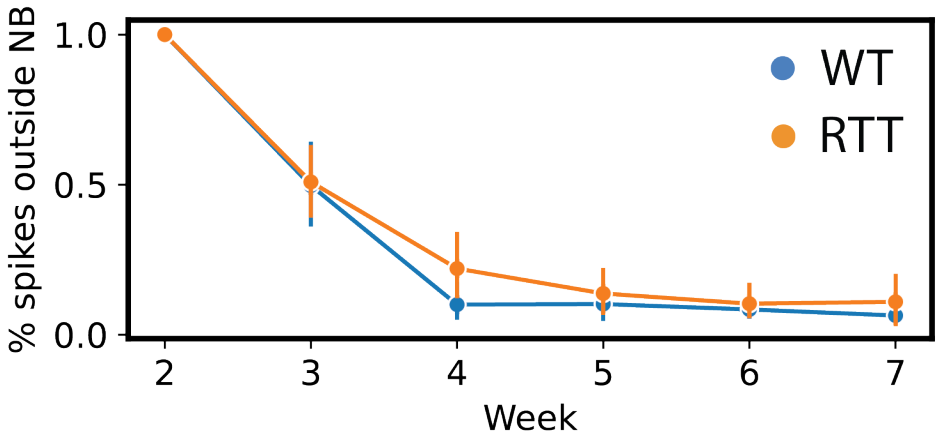

Figure SR1. The proportion of inter-burst spiking activity. *MECP2* mutant and wildtype networks. Network activity first formed with a high degree of inter-burst spiking activity that decreased over development.

1.2 Inconsistent handling and detection of RSBs

1.2.1 Standard ISI-based burst detection algorithms

Top of document

Fixed ISI network burst detection was highly susceptible to the experimenter's choice of parameters compared to adaptive ISI network burst detection. Boundaries around bursts (i.e., the start and end of bursts) were sensitive to parameter choice and burst detection method (Figure SR2).

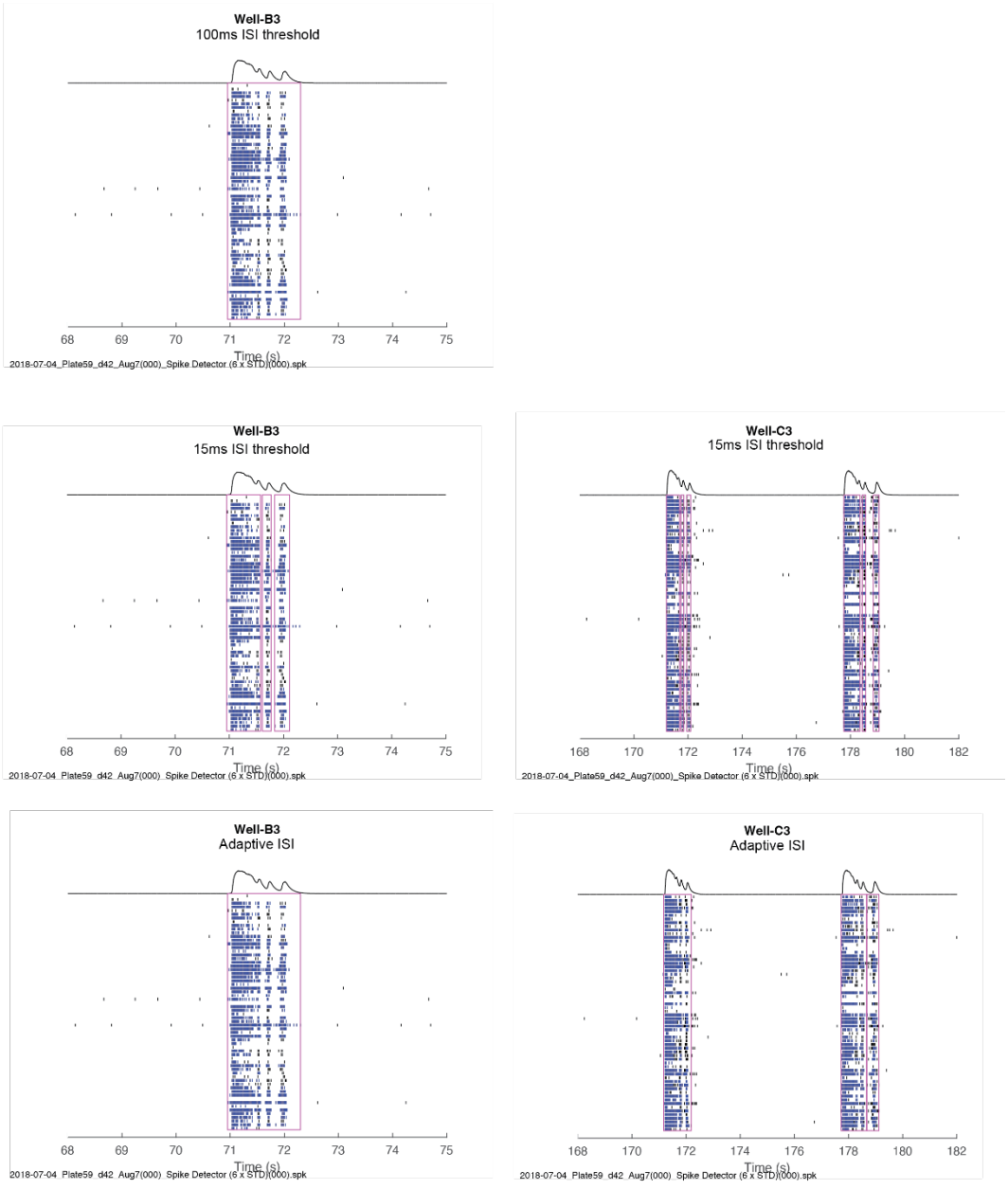

Figure SR2. Inconsistent burst boundaries by ISI-based burst detection algorithms.

Differences in burst boundaries produced significant differences in burst features such as network burst frequency (One-way ANOVA, $F(2,41) = 23.034$, $p < 0.001$, Figure 3A *top*) and network burst duration (One-way ANOVA, $F(2,17.048) = 12.640$, $p < 0.001$, Figure 3B *bottom*). Interestingly, post hoc comparison for network burst frequency revealed that adaptive ISI burst detection was not significantly different compared to 100ms ISI fixed-based burst detection ($p_{bonf} = 0.585$), whereas 15ms ISI fixed-based burst detection was significantly different from both adaptive and 100ms ISI fixed-based methods ($p_{bonf} < 0.001$, $p_{bonf} < 0.001$, respectively). On the other hand, post hoc comparison for network burst duration revealed our choice of adaptive-based burst detection was significantly different compared to 100ms ISI fixed-based burst detection ($p_{bonf} = 0.024$) but not 15ms ISI fixed-based burst detection ($p_{bonf} = 0.079$). Again, 15ms ISI fixed-based burst detection significantly differed from the 100ms ISI fixed-based burst detection ($p_{bonf} < 0.001$). Based on this, the adaptive ISI burst detection method determines burst boundaries variably either around the entire RSBs or the individual mini-bursts, which would therefore impact the reliability of downstream bursting metrics.

1.2.2 PSD burst frequency detection

We also conducted a similar Welch power spectral density (PSD) estimate seen in Mok et al. (2022)(1). This approach enables the characterization of the frequency components of the network's spike trains. PSD detected the burst frequency in both reverberating and non-reverberating networks (Figure 3B *red dot*); however, could not estimate the faster reverberation frequency of mini-bursts (Figure 3b *bottom red arrow*).

1.2.3 Reverberating super burst detection

Using the network-level SDF (Figure 3C), we identified local activity peaks that met a criterion (see Supplementary Materials and Methods 4.8, Figure 3D). Local activity peaks mapped onto network bursts with a sufficient firing rate (Figure 3D, E). Inter-burst-peak-interval (IBPI), the time between subsequent local activity peaks, approximated IBI. IBPI was used in reverberating network detection because it offered an adequate approximation of IBI that was unbiased by the calculation of the burst's boundaries (Figure 3F). This approach is useful in the detection of RSBs because burst boundary detection is non-trivial when the network burst firing rate does not reach an arbitrarily low threshold before increasing again – the case in some RSBs (Figure 3D). The amplitude of the peak represented the maximum firing rate of each network burst (Figure 3D). Amplitude was used to label bursts as either initiation network bursts or mini-bursts (Figure 3D, E). IBPI was used to determine when bursts were part of or outside of RSBs (see R_{max} calculation under Supplementary Materials and Methods 4.8.4).

Reverberating networks were identified by plotting the amplitude of the detected bursts against their frequency (IBPI). Reverberating networks show two clear clusters (Figure 3G). The first cluster was found to populate the high firing rate and long IBPI dimensions. This represented the large amplitude initiation network burst and the corresponding long interval to the mini-burst of the previous RSB (Figure 3G *green dots in the scatter plot*). The second cluster populated to low firing rate mini-bursts and low-to-medium IBPI to the previous mini-burst or to the large initiation burst within an RSB (Figure 3G *red dots in the scatter plot*).

In non-reverberating networks, our analyses often produced a single continuous cluster (Figure 3H *green dots in the top scatter plot*). The single cluster was tightly constrained to a narrow range, representing a highly periodic network with regular IBPIs and a similar maximum firing rate

within each network burst. Occasionally, in some networks, where the amplitude of the maximum firing rate for each network burst was highly variable, two clusters would appear but overlap strongly along the IPBI dimension (Figure 3H *green dots in the bottom scatter plot*). Since the frequency of mini-bursts is essential to reverberations we only considered reverberating networks when clusters could be distinguished along the IPBI dimension or along both dimensions (Figure 3G). The latter was an appropriate method since we rarely found clusters that segregated along the IBPI dimension but not along the firing rate dimension.

This approach allowed us to categorize networks as reverberating or non-reverberating. Furthermore, labels and parameters were extracted to identify the types of bursts (e.g., initiation network burst vs. mini-burst, Figure SR3) and the threshold to adaptively define boundaries around RSBs for subsequent feature calculation (see Supplementary Materials and Methods 4.9 and Figure S3 for algorithm block diagram).

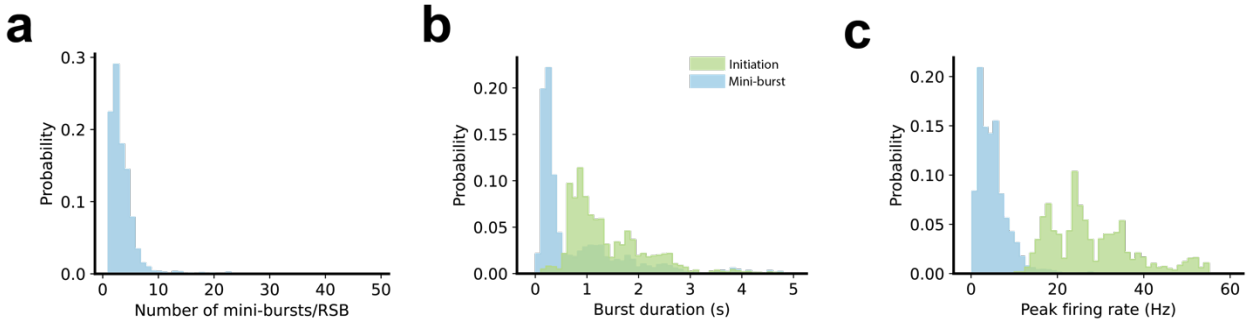

Figure SR3. Initiation burst versus mini-burst of reverberating networks.
(a) Distribution of the number of mini-bursts per RSB, (b) initiation burst (green) and mini-burst (blue) duration, and (c) initiation burst (green) and mini-burst (blue) peak burst firing rate.

1.3 *MECP2* null networks reverberate more than isogenic control networks

1.3.1 Network Reverberation Index

We introduced the Network Reverberation Index (NRI) metric to describe this variable distribution between isogenic pairs (see NRI calculation in Supplementary Materials and Methods 4.9.2). A positive NRI means that the *MECP2* mutant network contains more RSBs than isogenic controls. A negative NRI means the opposite and a zero NRI means they contain the same number of RSBs.

We show that WIBR3 null networks consistently show higher NRI values relative to isogenic controls networks (Figure 4B) during the middle (weeks 4 and 5) to late (week 6 and 7) stages of development (Kruskal-Wallis, $H(1) = 16.653$, $p < 0.001$, Figure 4A *left*). For PGPC14 null networks, the NRI values also showed a higher proportion of reverberating networks compared to their controls (Figure 4A *right*, B) but these were not significantly different from isogenic pairs (Kruskal-Wallis, $H(1) = 0.419$, $p = 0.517$) due to the low numbers of reverberating networks. The NRI values close to zero or less for the CLT mutant networks showed no significant differences in the proportion of RSBs relative to isogenic controls (Kruskal-Wallis, $H(1) = 2.344$, $p = 0.126$, Figure S4).

1.3.2 Burst hyperactivity

Post hoc pairwise comparison between WIBR3 wildtype controls and null groups at specific developmental time points revealed the number of network bursts was significantly increased relative to isogenic controls during week 6 ($p_{bonf} < 0.001$) and 7 ($p_{bonf} = 0.018$) (Figure 4C).

Top of document

1.4 RSBs bias the calculation of burst metrics

1.4.1 Network event duration and frequency

Network event duration was significantly different between WIBR3 NR-WT, NR-NULL, and R-NULL groups (Two-way ANOVA, $F(2,250) = 72.051$, $p < 0.001$, Figure 5B) and between different developmental time points (Two-way ANOVA, $F(4,250) = 22.577$, $p < 0.001$, Figure 5b), with a significant interaction (Two-way ANOVA, $F(8,250) = 13.983$, $p < 0.001$). Post-hoc comparison revealed burst duration in NR-WT and NR-NULL were not significantly different ($p_{bonf} = 0.788$), whereas R-NULL was significantly different from NR-NULL ($p_{bonf} < 0.001$) and NR-WT ($p_{bonf} < 0.001$). Thus, network event duration was longer in R-NULL, which would be anticipated if such events are RSBs.

Network event frequency was significantly different between NR-WT, NR-NULL, and R-NULL groups (Two-way ANOVA, $F(2,252) = 34.095$, $p < 0.001$, Figure 5C) and between different developmental time points (Two-way ANOVA, $F(4,252) = 4.464$, $p < 0.01$, Figure 5C), with a non-significant interaction (Two-way ANOVA, $F(8,252) = 1.674$, $p = 0.105$, Figure 5C). Post-hoc comparison revealed all groups were statistically different from each other (NR-NULL*R-NULL: $p_{bonf} < 0.05$; NR-NULL*NR-WT: $p_{bonf} < 0.001$; R-NULL*NR-WT: $p_{bonf} < 0.001$). The NR-NULL networks had significantly lower network event frequency compared to the NR-WT networks, unlike network event duration which did not show a significant difference (Figure 5B, C). However, the lowest network event frequency was in the R-NULL networks (Figure 5C). The latter would be also anticipated in networks that show an increase in RSBs.

1.4.2 RSB features

To quantitatively explore the factors that influenced the changes in RSB duration and RSB frequency in reverberating networks, we examined the reverberating mini-burst activity in both reverberating WIBR3 wildtype (R-WT) and null (R-NULL) networks that only had RSB network events. We found that as the R-NULL networks developed, they consistently had elevated numbers of mini-bursts per RSBs compared to the R-WT networks (Kruskal-Wallis, $H(1) = 35.126$, $p < 0.001$, Figure 5D). The peak of reverberating activity occurred during week 5. Similarly, R-NULL networks have significantly longer RSB duration relative to controls (Kruskal-Wallis, $H(1) = 451.899$, $p < 0.001$, Figure 5E). Through linear regression, we found that the longer RSBs duration in all R-NULL networks was positively correlated with an increased number of mini-bursts per RSBs (Pearson correlation coefficient $r = 0.788$, $p < 0.001$, Figure 5F).

Furthermore, we calculated the mini-burst frequency within each RSB. We found that mini-burst frequency was significantly elevated in R-NULL compared to isogenic R-WT networks (Kruskal-Wallis, $H(1) = 10.204$, $p = 0.001$). The mini-burst frequency peaked during week 6 and subsequently decreased during week 7 (Figure 5G). Taken together, that change in RSB duration (Figure 5E), which decreased by 2-fold in R-NULL networks after week 5, was likely due to decreased number of mini-bursts per RSB (Figure 5D) and increased mini-burst frequency (Figure 5G). Importantly, these results show that even if RSB were not exclusively found in R-NULL networks, their features were different from those found in R-WT networks suggesting that MECP2 deficiency exacerbates RSBs.

Top of document

1.5 GABA antagonism does not affect RSBs

A previous study reported that reverberations in stem cell-derived organoids were sensitive to the application of Bicuculline, a GABA antagonist(2). This seems at odds with our results since our monolayer networks were composed of excitatory neurons(1). To investigate this issue, we performed new MEA studies on the WIBR3 excitatory networks, since these lines were the ones showing stronger RSBs. Notably, in this separate experiment, we validated the previously discussed skew of RSBs towards the null networks, with very few control networks exhibiting RSBs.

Application of bicuculline in non-reverberating control (NR-WT) and reverberating null (R-NULL) excitatory networks had no effect on the presence of RSBs (Independent Samples Student T, $t(32) = -1.123$, $p < 0.270$, Figure 6A, B). Interestingly, in both bicuculline-treated networks, there was a non-significant increase in network event frequency (Independent Samples Student T, $t(32) = -1.735$, $p = 0.092$, Figure 6C). Network event duration was similarly found to be unaffected by bicuculline in either networks (Mann-Whitney, $p = 0.746$, Figure 6D). The subtle effects in the former may be due to off-target effects of bicuculline on membrane channels such as small conductance calcium-activated potassium channels which is responsible for the slow afterhyperpolarization of neurons after action potential firing (3,4). Notably, a subtle increase in mini-burst frequency was found between pre- and post-bicuculline-treated R-NULL (Mann-Whitney, $p < 0.05$, Figure 6E). These results corroborate our networks were predominantly excitatory, and bicuculline had limited effect on RSBs.

1.6 RSBs are dependent on asynchronous Ca^{2+} release

DMSO provided an additional control for the possible effects of experimental manipulations on the network activity. EGTA-AM treatment eliminated RSB in mutant networks. Remarkably, we found no significant differences in the presence of RSBs between post-treatment EGTA-NULL and DMSO-WT groups (Kruskal-Wallis, Dunn's post hoc, $p_{bonf} = 0.902$, Figure 6M). Network event frequency was not significantly different between post-treatment EGTA-NULL and DMSO-WT (Kruskal-Wallis, Dunn's post hoc, $p_{bonf} = 0.360$, Figure 6N). Network event duration was similarly not significantly different between post-treatment EGTA-NULL and DMSO-WT (Kruskal-Wallis, Dunn's post hoc, $p_{bonf} = 0.075$, Figure 6O). Both mean ISI within network event (Kruskal-Wallis, Dunn's post hoc, $p_{bonf} = 1.000$, Figure 6P) and median/mean ISI within network event (Kruskal-Wallis, Dunn's post hoc, $p_{bonf} = 1.000$, Figure 6Q) were not significantly different between post-treatment groups (EGTA-NULL and DMSO-WT), indicating both networks had similar firing rate distributions (as ISI is the inverse of firing rate).

1.7 EGTA-AM decreases the duration of the initiation network burst

Network burst duration in EGTA treated null (EGTA-NULL) networks were significantly shorter than control networks without EGTA-AM (preEGTA-WT) treatment (Kruskal-Wallis, Dunn's post hoc, $p_{bonf} = 0.026$) but not significantly different from WT with EGTA (EGTA-WT) networks (Kruskal-Wallis, Dunn's post hoc, $p_{bonf} = 0.663$, Figure 7B). Furthermore, EGTA-WT and preEGTA-WT were not significantly different from each other (Kruskal-Wallis, Dunn's post hoc, $p_{bonf} = 0.456$, Figure 7B). These results are more easily seen in Figure 7C, where the SDFs for the burst of pre- and post-EGTA treatment in control and nulls are overlaid on top of each other. A stark difference can be seen when comparing EGTA-NULL and preEGTA-NULL. Along the same

lines, we found that the initiation burst duration was significantly reduced in EGTA-NULL compared to preDMSO-WT (Kruskal-Wallis, Dunn's post hoc, p_{bonf} = 0.011, Figure 7D) and DMSO-WT (Kruskal-Wallis, Dunn's post hoc, p_{bonf} = 0.031, Figure 7D).

2 Supplementary Figures

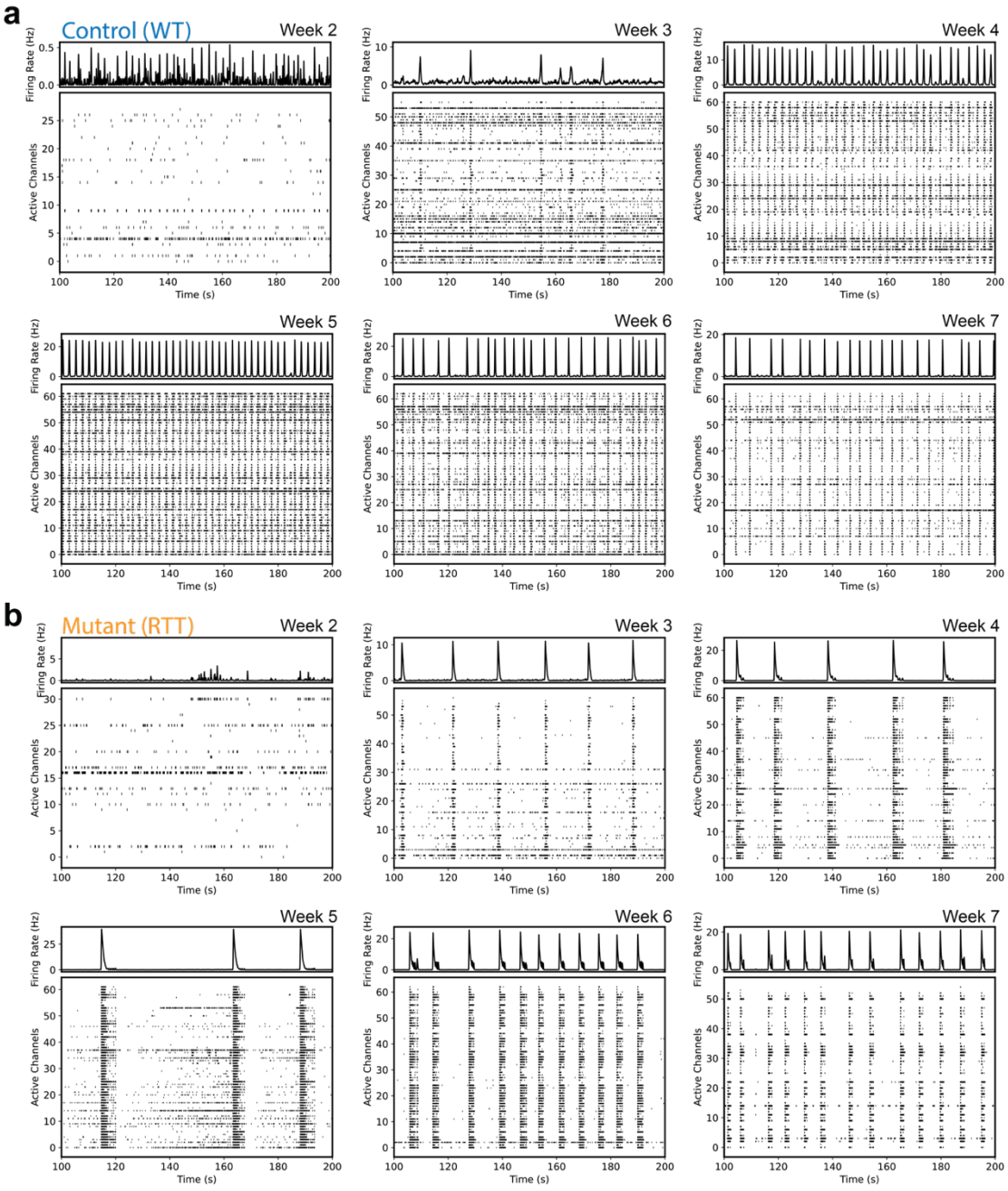

Figure S1. Development of *MECP2* WT and mutant networks.

(a-b) Raster plots for each developmental time point from representative (a) wildtype and (b) *MECP2* mutant networks. The top subplot is the network-averaged spike density function representing the estimated instantaneous firing rate of the network.

Top of document

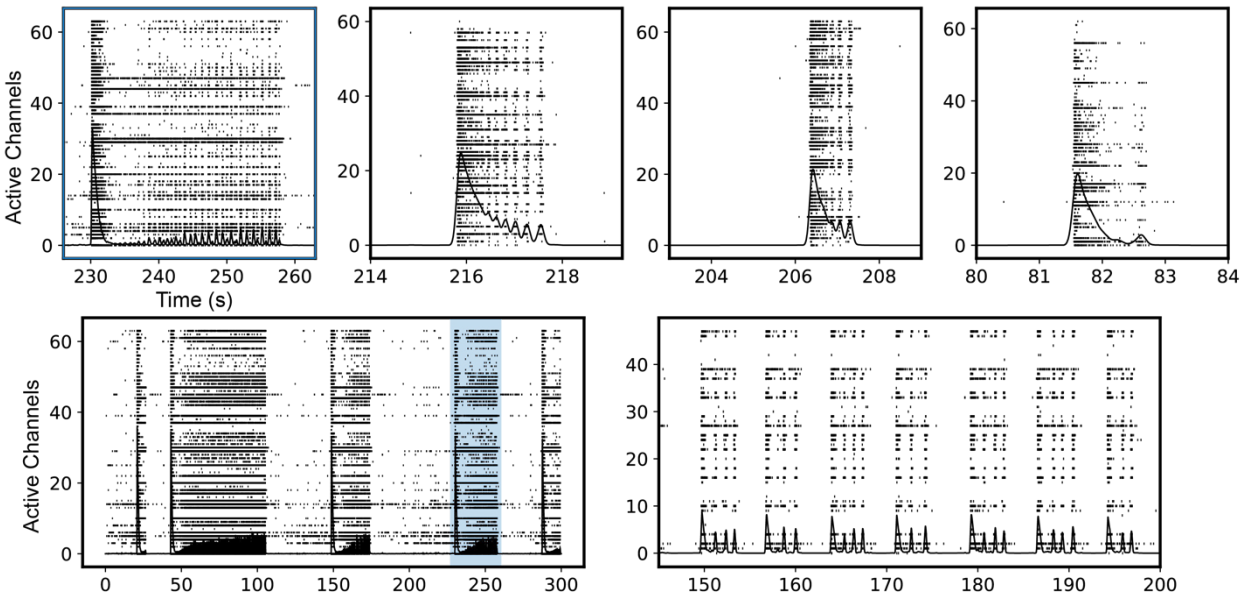

Figure S2. Selected examples of spike density function overlaid on raster plots demonstrating the diversity of reverberating super burst patterns.

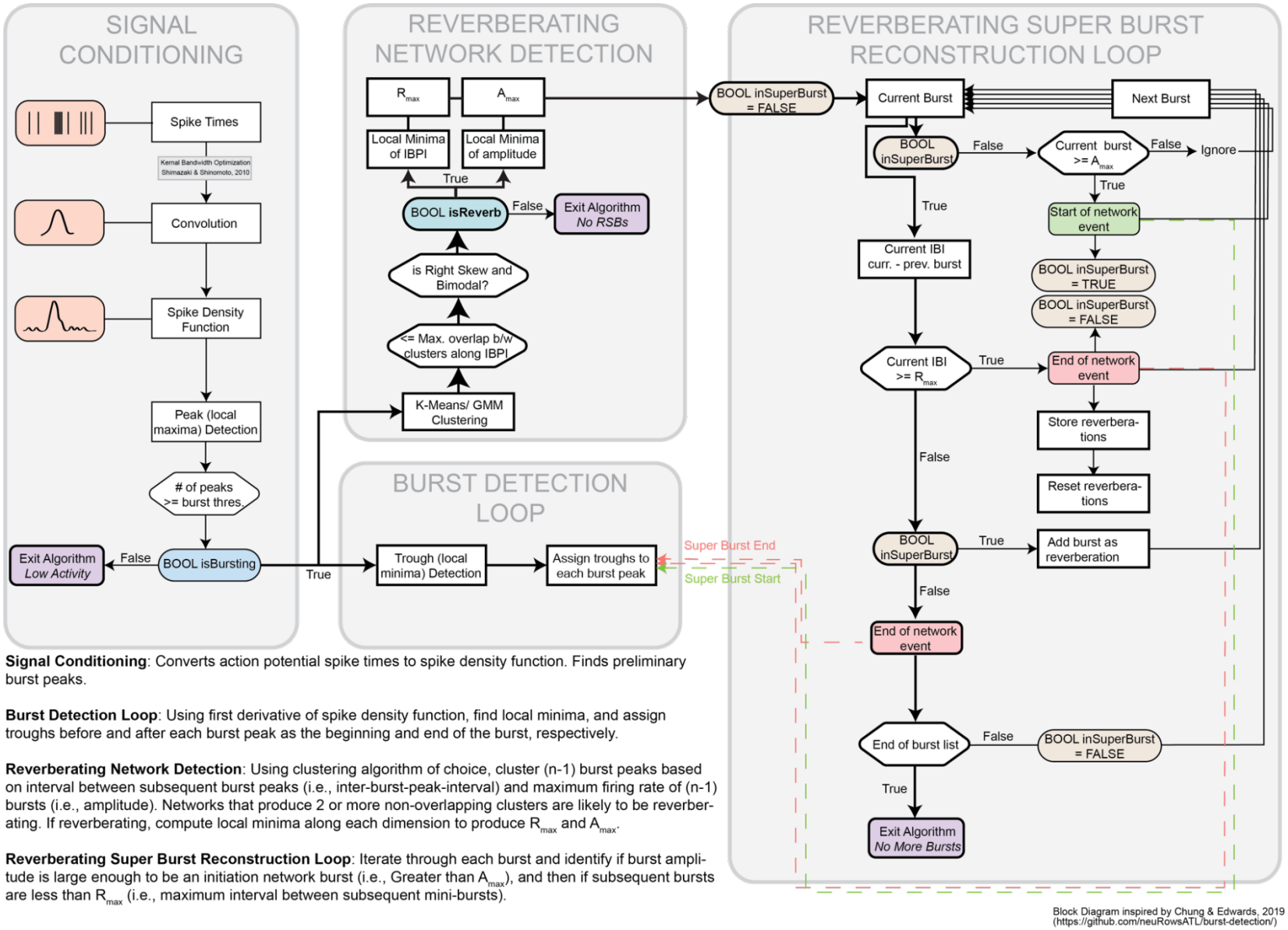

Signal Conditioning: Converts action potential spike times to spike density function. Finds preliminary burst peaks.

Burst Detection Loop: Using first derivative of spike density function, find local minima, and assign troughs before and after each burst peak as the beginning and end of the burst, respectively.

Reverberating Network Detection: Using clustering algorithm of choice, cluster (n-1) burst peaks based on interval between subsequent burst peaks (i.e., inter-burst-peak-interval) and maximum firing rate of (n-1) bursts (i.e., amplitude). Networks that produce 2 or more non-overlapping clusters are likely to be reverberating. If reverberating, compute local minima along each dimension to produce R_{max} and A_{max}.

Reverberating Super Burst Reconstruction Loop: Iterate through each burst and identify if burst amplitude is large enough to be an initiation network burst (i.e., Greater than A_{max}), and then if subsequent bursts are less than R_{max} (i.e., maximum interval between subsequent mini-bursts).

Figure S3. Block diagram of Burst Reverberation Detection algorithm

Top of document

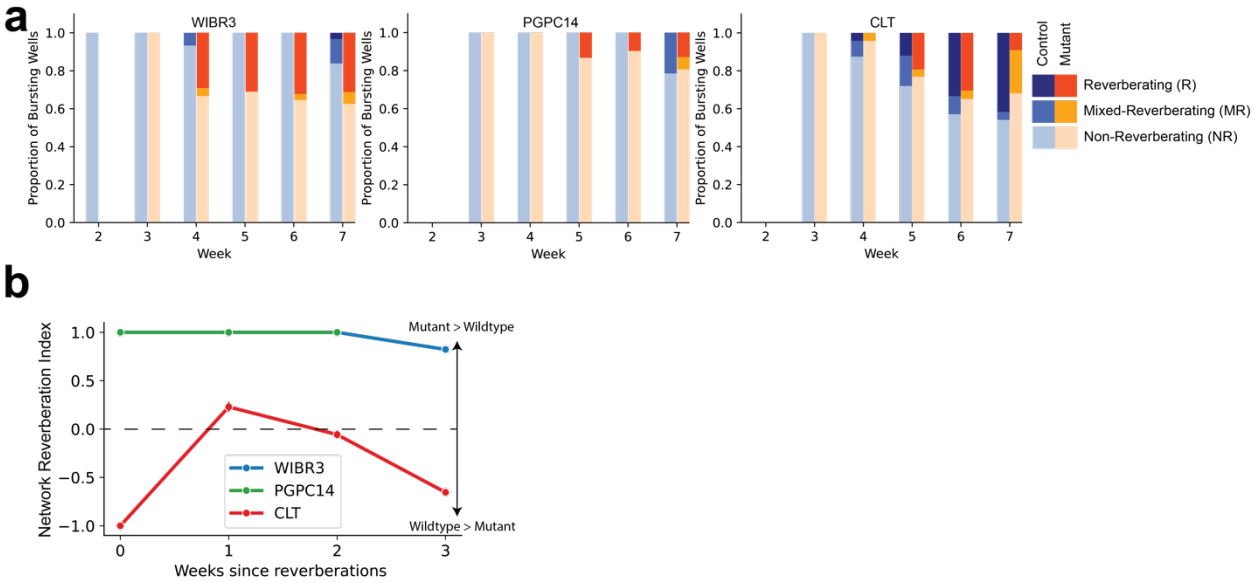

Figure S4. *MECP2* null networks reverberate more than isogenic controls and exhibit greater bursting activity, indicating hyper-activity.

(a) Proportion of reverberating, mixed-reverberation, and non-reverberation wells relative to the total number of bursting wells across development for each individual.

(b) Network Reverberation Index, representing the plate-matched difference in proportion of reverberating networks for each individual.

Top of document

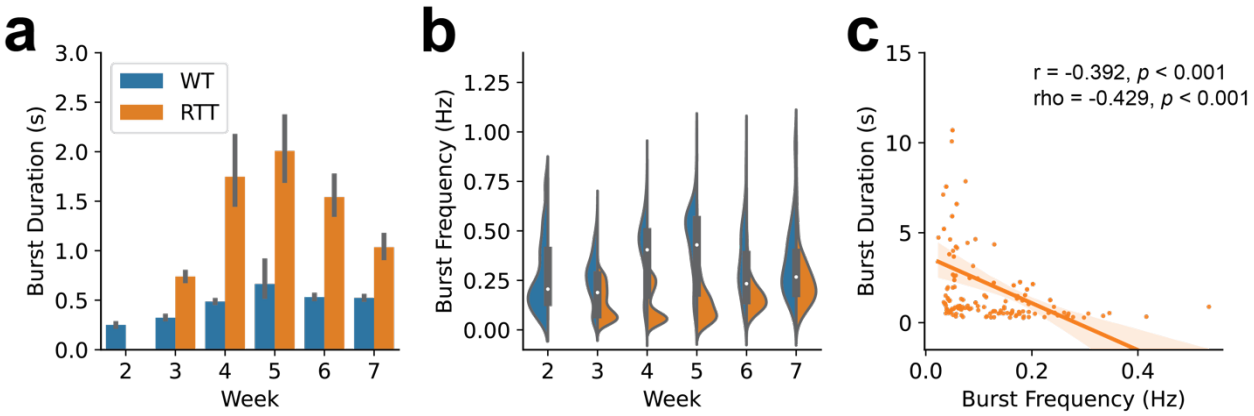

Figure S5. Replication of Mok et al. (2022) with SDF-based Network Burst Detection.

Top of document

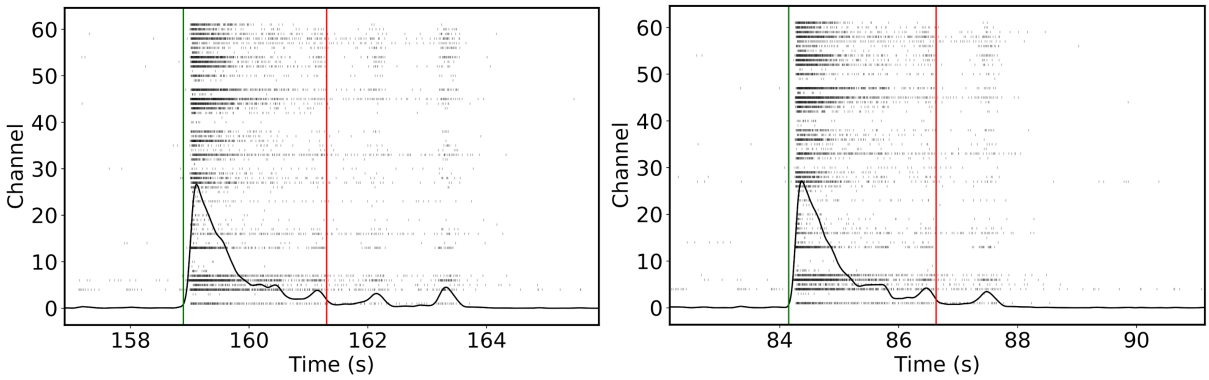

Figure S6. Very long initiation bursts are the result of the first mini-burst merging with the initiation burst. Green line indicates start of initiation burst. Red line indicates end of initiation burst.

3 Supplementary Discussion

3.1 Single neuron and network excitability in MECP2 null neurons

3.1.1 Hyperexcitable bursting activity

A somewhat contradictory finding was that despite this hyperexcitability in single neurons, network burst frequency in *MECP2* null networks was originally determined by standard burst detection algorithms to be decreased(1). Specifically, the *MECP2* null networks showed a decreased number of network bursts, increased network burst duration, and decreased network burst frequency(1). These findings were interpreted as a decrease in network excitability. But how can hyperexcitable *MECP2* null neurons produce a hypoexcitable phenotype? Here, we zoomed into the long bursts of *MECP2* null neurons and found a phenomenon we termed reverberating super bursts (RSB). RSBs are network events classified as single network bursts using standard burst detection algorithms. However, using our algorithm we show that RSBs are truly composed of an initial prolonged large amplitude burst followed by several mini-bursts occurring at a high frequency. This pattern resembles reverberations such as those observed in 'epileptic' networks(5–7). When RSBs and the containing mini-bursts were factored in, *MECP2* null networks demonstrated increased total number of network bursts, consistent with the hyperexcitability phenotype seen in single neurons. Thus, hyperexcitable *MECP2* null neurons led to a hyperexcitable bursting phenotype characterized by the network's propensity to generate reverberatory bursting activity.

3.1.2 Mean firing rate still indicates hypoactivity?

Another contradictory finding with this was the report of reduced mean firing rate (MFR) in *MECP2* null networks, indicating hypo-activity. However, single *MECP2* null neurons can be

hyperexcitable (indicated by lower rheobase or threshold for evoking action potentials) and still fire trains with fewer spikes relative to wildtype control neurons. Taken together,

3.2 Mechanisms of RSB generation

3.2.1 E-I mechanism

Abnormalities in the excitation/inhibition balance have been proposed by a study in brain organoids containing a mix of excitatory and inhibitory neurons(2). The use of bicuculline, a $GABA_A$ receptor antagonist, decreased the number of RSBs (referred to as nested oscillations in the study(2)) while preserving network bursts. Therefore, the authors proposed that the interplay between inhibitory and excitatory synapses was the likely source of RSBs. However, in our study, the networks did not contain inhibitory interneurons, and we still observed RSBs, that were more frequent in *MECP2* null neurons. Moreoever, we used bicuculline and found no effect on RSBs.

3.2.2 Calcium mechanism

The application of EGTA-AM had robust effects in eliminating RSBs, strongly implicating slow-kinetic calcium dynamics in maintaining RSBs. EGTA-AM can enter the synaptic terminal causing a decrease in asynchronous neurotransmitter release without affecting the large, localized Ca^{2+} transients responsible for synchronous release(8,9). Importantly, EGTA-AM was further shown to restore burst phenotype metrics in reverberating networks to similar levels as isogenic controls.

One possible explanation for these results is that RSBs are maintained by elevated Ca^{2+} in the presynaptic terminal, which triggers asynchronous neurotransmitter release(10). Asynchronous release occurs when Ca^{2+} levels remain elevated even after the initial stimulus has ended, typically after moderate to high-frequency stimulation(10,11). Lau and Bi suggest that asynchronous neurotransmitter release plays crucial roles in the sustained persistence of activity after transient

inputs – implicating its function in working memory and motor planning circuits and demonstrating numerous mechanisms further implicated in maintaining reverberating-like activity(12,13). Dao Duc et al. suggested reverberating-like activity would be detectable as changes in amplitude of excitatory postsynaptic currents evoked by paired stimuli with a short inter-stimulus-interval, reminiscent of Lau and Bi's paired-pulse protocol that replicated reverberating-like activity(11,12). The decrease in rheobase observed in the *MECP2* null neurons of our study may also contribute to the recruitment of voltage-sensitive Ca^{2+} channels in the presynaptic terminal and its availability to trigger asynchronous neurotransmitter release(14).

3.2.2.1 Long initiation bursts and their consequence

Reverberating networks had a more prolonged initiation burst duration compared to non-reverberating network mean burst duration. EGTA-AM treatment reduced initiation burst duration in reverberating networks, suggesting the association that the longer initiation burst duration may produce elevated presynaptic Ca^{2+} build-up, which would trigger reverberating mini-bursts in genetically predisposed hyperexcitable neurons. It is likely that *MECP2* null networks exist in a hyperexcitable state, such that physiologically relevant stimuli are more likely to trigger a network reverberation. RSBs may serve as a predisposing factor for the development of disorders of hyperexcitability such as epilepsy which has been shown to have numerous etiologies(6,15,16). Reverberations can induce long-term potentiation in synapses and trigger mechanisms of synaptic plasticity(10,13,17,18). During the early stages of network development, such mechanisms are critical for forming connections between neurons and establishing different modes of network dynamics. One possibility is that RSBs serve as a compensatory mechanism for *MECP2* null networks to achieve similar levels of connectivity as typically developed networks. However, this

persistent excitation coupled with hyperexcitability may contribute to the development of seizures – a comorbidity observed in RTT patients(6,15).

3.2.3 Connectivity mechanism

At early time points, networks are weakly connected, and excitatory inputs may be insufficient to produce successive rounds of reverberating mini-bursts. As synaptic strength increases, this will permit noisy asynchronous neurotransmitter release to elicit RSBs. Over time, the rapid and strong initiation burst in these RSBs would deplete neurons of neurotransmitter resources, precluding additional rounds of reverberating mini-bursts and establishing mature bursting dynamics.

3.3 CLT phenotype

Interestingly, the CLT phenotype did not show the increase in single neuron excitability nor the clear increase in network excitability(1) observed in the *MECP2* null phenotypes (WIBR3 and PGPC14), suggesting that RSBs dominating network dynamics may be linked to the more severe *MECP2* mutations(19). The CLT phenotype was not hyperexcitable nor showed significant differences in AMPAR-mEPSC amplitude or frequency, alongside no changes in synaptic density(1). In contrast, the *MECP2* null phenotype was reduced across the board(1). It may be that the CLT phenotype does not have the same magnitude of changes underlying connectivity to demonstrate the differences in RSBs compared to the *MECP2* null mutants.

4 Supplementary Materials and Methods

4.1 Cell culture and differentiation

Three human-derived stem cell lines were previously generated. Briefly, CLT L124W mutant iPSC lines were derived from fibroblasts of a clinically diagnosed Rett Syndrome patient. WIBR3 was derived from an unaffected ESC line, and PGPC14 was from an unaffected iPSC line. Using XCI assays, isogenic control pair for the CLT line was identified. Gene editing was used to generate isogenic null mutant pairs for the unaffected lines (WIBR3, PGPC14). *Neurogenin-2* (*Ngn2*) overexpression protocol rapidly differentiated hSC lines towards excitatory cortical neurons. All cell lines were examined for MECP2 protein levels. For further information, refer to Mok et al. (2022)(1).

4.2 MEA plating and recording

MEA plating was performed as previously described in Mok et al. (2022)(1). Briefly, 12-Well Cytoview plates (Axion Biosystems) containing 64 electrodes per well were coated with sterilized 0.1% PEI solution in borate buffer solution pH 8.4 for 1 hour at room temperature. Plates were then washed 4 times with sterile water and allowed to dry overnight. Day 8 Ngn2 neurons were then seeded at a density of 100,000 cells per well in 100 µl droplets of CM2 Brainphys media [Brainphys (STEMCELL technologies), 1x Glutamax, 1x pen/strep, 10 ng/ml BDNF, 10 ng/ml GDNF], supplemented with 400 µg/ml laminin and 10 µM ROCK inhibitor. Seeded cells were allowed to settle for 2 hours to ensure good adherence to the recording surface before wells were carefully flooded with an additional 1 ml of CM2 Brainphys media, supplemented with 40µg/ml laminin. The following day, P1 mouse astrocytes were added to each well at a seeding density of 20,000 cells per well, maintaining a 5:1 ratio of neurons to astrocytes. Cell culture media was changed twice weekly during the recording schedule, with media changes occurring exactly 24

hours prior to each recording, with the exception of pharmacological treatment experiments (see Pharmacological treatments). For MEA recordings, each plate was allowed to incubate for 5 minutes on an Axion Maestro device heated to 37°C under 5% CO_2. Spontaneous activity was then recorded at a sampling frequency of 12.5 kHz for 5 minutes using AxIS v2.0 software, with the analog filter settings set to "Neural: Spikes" mode (1200X gain, 200 – 5000 Hz bandwidth, median referencing). Neural spikes recordings were further bandpass filtered at 0.2 – 3 kHz and spikes were detected using a threshold crossing method with the threshold set at 6x the standard deviation of the noise of recording electrodes. Further analyses of recorded spikes were performed in Python (https://www.python.org).

4.3 Pharmacological treatments

MEA plates were recorded twice weekly as described in MEA Plating and Recording and were monitored for the appearance of RSBs. Pharmacological treatments began after RSBs were detected in cultures. Before adding any pharmacological compounds, culture media was first changed with fresh CM2 media and plates were allowed to incubate for 1 hour to allow neuronal activity to stabilize. Baseline spontaneous activity was then recorded for 10 minutes at 37 °C. Immediately following baseline recording, one pharmacological agent (0.1% DMSO, or 10 µM bicuculline) was added to each well and 10 minutes of post-treatment spontaneous activity was recorded. Culture media was then changed 3 times to washout pharmacological agents and plates were allowed to incubate for another hour to allow activity to stabilize. A new 10-minute baseline recording was then taken, and the process was repeated until all pharmacological agents had been tested. 25 µM EGTA-AM was always added as the final drug compound in the rounds of testing as it was observed that normal baseline spontaneous activity did not return even after drug washout.

4.4 Intracellular Adaptation

To quantify adaptation in the intracellular current clamp recordings, spike times were first detected using Allen Institute's Intrinsic Physiology Feature Extractor (IPFX) Python package (https://github.com/AllenInstitute/ipfx). Action potential spike times across each current injection sweep was organized into 0.05s bins, producing the distribution of spike times for each neuron at all stimulation currents. Using SciPy's non-linear least squares curve_fit() function (https://docs.scipy.org/doc/scipy/reference/generated/scipy.optimize.curve_fit.html), a mono-exponential decay function was fitted using the equation below:

$$S(t) = S_0 e^{-\lambda t} + b$$

where *S(t)* represents the number of spikes at a given time (*t*). S_0 is the initial amount at $t = 0$. *e* is Euler's constant. λ is the rate of decay. *b* represents the baseline of spiking activity, at any given time.

4.5 ISI Threshold Burst Detection

All ISI-based burst detection was performed using Axion Biosystem's Neural Metrics tool (v2.2.4) using AxIS (2.0) software generated AxIS Spike (.spk) files. 15ms fixed ISI burst detection used a 15ms max ISI threshold with requirements of a minimum of 50 spikes and 35% of electrodes active. 100ms fixed ISI burst detection used a 100ms max ISI threshold with requirements of a minimum of 50 spikes and 35% of electrodes active. Adaptive ISI required a minimum of 50 spikes and 35% of electrodes active. The resulting Neural Metrics feature statistics were exported to a CSV file, compiled, and then analyzed using custom-built Python code.

4.6 Power Spectral Density Estimation

Spike times from each electrode were converted into a binary spike matrix with a bin size of 0.00008 seconds (i.e., 1/12.5kHz sampling frequency). Each electrode's spike matrix then underwent power spectral density (PSD) estimate using SciPy's welch() function (https://docs.scipy.org/doc/scipy/reference/generated/scipy.signal.welch.html) and expressed in decibels (dB) as a ratio against the PSD of a randomly permuted version of the same spike matrix. Each channel's PSD was averaged to generate the network-averaged PSD, representing the network's frequency components. Peaks in the spectra between 0Hz and 1Hz typically represented network burst frequency, whereas mini-burst frequency was expected to be between 1Hz and 10Hz.

4.7 Spike sorting

Individual neuronal units were identified from extracellular multielectrode arrays according to Axion Biosystem's Spike Sorting Protocol(20,21). In brief, multi-unit action potentials were extracted from raw voltage signals using AxIS Navigator (Axion Biosystems) and stored as an AxIS Spike (.spk) file (see MEA Plating and Recording). AxIS Spike files were converted to NeuroExplorer (.nex) file using Axion Data Export Tool. NeuroExplorer files were loaded into Plexon Offline Sorter (version 4.5.0). All channels underwent Automatic Sorting using a K-Means Scan with a range of 1 to 6. All spike sorting results underwent manual quality control(20). As a result of quality control, only 10% of the recordings could be considered single-unit spikes. 90% of the recordings were classified as multi-unit activity. This difficulty in spike sorting likely arises from a large electrode size, low impedance, and relatively low sampling frequency. Consequently, the quality of the single-unit isolation makes it very difficult to perform extensive analyses that rely on firing rate patterns.

4.8 Reverberating Super Burst Detection

See Supplementary Figure 3 for the algorithm block diagram.

4.8.1 Signal Conditioning

Spike times from each channel were converted to a binary spike matrix with bin sizes of 0.00008 seconds (i.e., 1/12.5kHz sampling frequency). Each spike matrix was convolved with a bandwidth-optimized Gaussian kernel(22) to generate a spike density function, representing the estimated instantaneous firing rate of each channel. The average instantaneous firing rate of the network was calculated by computing the spike count weighted average spike density function across all electrodes. Networks that did not exhibit a maximum instantaneous firing rate greater than 3Hz were excluded from the analysis, presumed to be non-bursting wells.

Network bursts were identified as having local maxima with a peak amplitude that exceeded a minimum burst threshold (10% of the maximum firing rate with a minimum of 3Hz). Additionally, burst peaks required a prominence of 50% of the maximum firing rate of the network. If the number of burst peaks exceeded 5 bursts, the analysis would proceed to the *Burst Detection Loop* and *Reverberating Network Detection*.

4.8.2 Burst Detection Loop

Preliminary burst boundaries, defining the start and end of network bursts, were calculated by finding the local maxima and minima of the first derivative of the spike density function. Local maxima represented the start of the burst, whereas local minima represented the end of the burst. Burst boundaries were assigned to previously calculated burst peaks that fell between the boundaries. In some instances, particularly between the initiation burst and the first mini-burst, it

was a challenge to locate the local minimum. This produced burst boundaries that overlapped, which, in a subsequent step, resulted in two or more bursts combining into a single, extended burst (Figure S6). This method occasionally resulted in longer-than-normal initiation bursts within reverberating networks.

4.8.3 Reverberating Network Detection

To identify reverberating networks, K-means clustering (and later Gaussian Mixed Models) was performed with amplitude (i.e., maximum firing rate) in *n*-1 burst and inter-burst-peak-interval between each burst (*n*).

Reverberating networks had two clearly defined clusters. The first cluster localized to the high inter-burst-peak-interval and high firing rate amplitude dimensions – representing the initiation network burst. The second cluster localized to the low inter-burst-peak interval and low firing rate amplitude dimensions – representing the mini-bursts.

Non-reverberating networks would exhibit one of the following:

1) One cluster: demonstrating a network that was highly periodic with low variability in the maximum amplitude of firing rate in each burst.
2) Two clusters: demonstrating a noisy network that contained maximum amplitude of firing rates that were highly variable, but often had periodic inter-burst-peak interval.

Based on this, the determining factor of a noisy versus reverberating network was minimal overlap across the both maximum firing rate and inter-burst-peak-interval dimensions, which was set to 20% overlap tolerance. Reverberating networks then proceeded to the *Reverberating Super Burst Construction Loop*.

4.8.4 Reverberating Super Burst Construction Loop

R_{max}, representing the maximum inter-burst-peak-interval within RSBs, was calculated by determining the local minima between the bimodal peaks seen along the inter-burst-peak-interval distribution of a reverberating network. A_{max}, representing the maximum firing rate of mini-bursts within RSBs, was calculated by determining the local minima between the bimodal peaks seen along the peak burst firing rate dimension.

Using the preliminary burst boundaries for all bursts that was previous calculated, and R_{max} and A_{max} parameters, new burst boundaries for RSBs were determined as followed. The start of every potential RSB always began with a network burst with an amplitude exceeding A_{max}. Once the initiation burst was found, if the difference between the start of the subsequent burst and the end of the current burst (i.e., inter-burst-peak-interval) was less than R_{max}, the subsequent burst was included into the RSB. This was repeated until the inter-burst-peak-interval was greater than R_{max} and the end of the RSB was marked.

Burst Reverberation Detection tutorial can be found on Github as well as the NDD-Ephys-dB (see 4.11): https://github.com/KartikP/Burst-Reverberation-Toolbox/tree/main/Tutorials

4.9 RSB Feature Analysis

The following are brief explanations for select features:

4.9.1 Initiation/First Burst Duration

Calculation of the first burst duration was non-trivial due to the variability in the firing rate pattern of the initiation network burst and the proceeding reverberating mini-bursts. For example, some initiation network bursts do not reach an arbitrarily low burst threshold until the end of the RSB, whereas others do, making traditional approaches to identifying boundaries for bursts inadequate.

To address this, we used the first derivative of the spike density function and identified local peaks and troughs which corresponded to changes in the firing rate velocity of the bursts, specifically the start and end of bursts, respectively. First burst duration was calculated by taking the time between the start and end of the initiation network burst.

4.9.2 Network Reverberation Index

Network Reverberation Index (NRI) was calculated for each reverberating developmental week using the following formula:

$$NRI = \frac{P_{Mutant} - P_{Control}}{P_{Mutant} + P_{Control}}$$

where P represents the proportion of reverberating networks for either mutant or control groups per individual per developmental week. NRI $\in$ (-1,1) and is positive when the mutant group is reverberating more and negative when the control group is reverberating more.

4.9.3 Network Event/Burst Duration

A network event was described as the entire RSBs (initiation network burst and mini-bursts) in reverberating networks or discrete single network bursts in non-reverberating networks. Network event duration was calculated as the average difference in time between the beginning and end of the boundaries of the network event for each well's recording.

4.9.4 Network Event/Burst Frequency

Network event frequency was calculated as the inverse of average inter-network-event-interval between subsequent network events.

4.9.5 Number of mini-bursts/RSB

The number of mini-bursts was calculated by counting non-initiation network burst peaks within the boundaries of the RSB.

4.9.6 RSB duration

Similar to *Network Event Duration*, RSB duration was calculated by calculating the difference in time between the beginning and end of the boundaries of each RSB.

4.9.7 Mini-burst frequency

Mini-burst frequency was calculated as the inverse of inter-mini-burst-interval.

4.10 RANSAC (RANdom Sample Consensus) Regression

Ordinary Least Squares (OLS) regression is sensitive to outliers. To generate a robust linear model for data that may contain outliers, Scikit-Learn's RANSACRegressor() function was used (https://scikit-learn.org/stable/auto_examples/linear_model/plot_ransac.html). RANSAC sampled a subset of the data (*min_samples = 50*), fitted a linear model (*estimator = LinearRegression()*) to the selected subset of data, evaluated the model (based on the number of inliers) and then repeated for a fixed number of iterations (*max_trials=100*). The model with the best consensus score (i.e., the number of points that fall within a threshold range and are therefore considered inliers) was selected. Where used, outlier data were plotted with increased transparency and excluded in the fit. Inlier data was plotted with decreased transparency and used to generate a linear fit of the data.

4.11 Data Availability (NDD-Ephys-dB)

The data can be found on NDD-Ephys-dB. The NDD-Ephys-dB is a resource for electrophysiological datasets and recordings explicitly related to human neurodevelopmental

disorders, including Rett Syndrome (RTT). The database contains in vitro data, including intracellular (.abf or .nwb file format) and extracellular (in Axion .spk, .csv, and HDF5 file formats) electrophysiological recordings. In addition to serving as a repository for electrophysiological data, the database provides tools like burst detection algorithms, visualization GUIs, and feature calculation toolboxes to assist with the exploration and investigation of data. NDD-Ephys-dB aims to promote data-sharing of published results and data-mining by computational neuroscientists. The goal is to expand the resource to include 3D and high-density MEA results to advance studies of all neurodevelopmental disorders.

5 Supplementary References

1. Mok RSF, Zhang W, Sheikh TI, Pradeepan K, Fernandes IR, DeJong LC, et al. Wide spectrum of neuronal and network phenotypes in human stem cell-derived excitatory neurons with Rett syndrome-associated MECP2 mutations. Transl Psychiatry. 2022 Oct 18;12(1):1–16.

2. Trujillo CA, Gao R, Negraes PD, Gu J, Buchanan J, Preissl S, et al. Complex Oscillatory Waves Emerging from Cortical Organoids Model Early Human Brain Network Development. Cell Stem Cell. 2019 Oct 3;25(4):558-569.e7.

3. Khawaled R, Bruening-Wright A, Adelman JP, Maylie J. Bicuculline block of small-conductance calcium-activated potassium channels. Pflugers Arch. 1999 Aug;438(3):314–21.

4. Johansson S, Druzin M, Haage D, Wang MD. The functional role of a bicuculline-sensitive Ca2+-activated K+ current in rat medial preoptic neurons. J Physiol. 2001 May 1;532(Pt 3):625–35.

5. Blumenfeld H. Cellular and Network Mechanisms of Spike-Wave Seizures. Epilepsia. 2005;46(s9):21–33.

6. McCormick DA, Shu Y, Hasenstaub A, Sanchez-Vives M, Badoual M, Bal T. Persistent Cortical Activity: Mechanisms of Generation and Effects on Neuronal Excitability. Cereb Cortex. 2003 Nov 1;13(11):1219–31.

7. Sanchez-Vives MV, McCormick DA. Cellular and network mechanisms of rhythmic recurrent activity in neocortex. Nat Neurosci. 2000 Oct;3(10):1027–34.

8. Nakamura Y. EGTA Can Inhibit Vesicular Release in the Nanodomain of Single Ca2+ Channels. Front Synaptic Neurosci. 2019;11:26.

9. Adler E, Augustine G, Duffy S, Charlton M. Alien intracellular calcium chelators attenuate neurotransmitter release at the squid giant synapse. J Neurosci. 1991 Jun 1;11(6):1496–507.

10. Kaeser PS, Regehr WG. Molecular Mechanisms for Synchronous, Asynchronous, and Spontaneous Neurotransmitter Release. Annu Rev Physiol. 2014;76:333–63.

11. Dao Duc K, Lee CY, Parutto P, Cohen D, Segal M, Rouach N, et al. Bursting Reverberation as a Multiscale Neuronal Network Process Driven by Synaptic Depression-Facilitation. PLoS ONE. 2015 May 27;10(5):e0124694.

12. Lau PM, Bi GQ. Synaptic mechanisms of persistent reverberatory activity in neuronal networks. Proc Natl Acad Sci U S A. 2005 Jul 19;102(29):10333–8.

13. Iremonger KJ, Bains JS. Integration of Asynchronously Released Quanta Prolongs the Postsynaptic Spike Window. J Neurosci. 2007 Jun 6;27(25):6684.

14. Catterall WA. Voltage-Gated Calcium Channels. Cold Spring Harb Perspect Biol. 2011 Aug;3(8):a003947.

15. Holcman D, Tsodyks M. The Emergence of Up and Down States in Cortical Networks. PLoS Comput Biol [Internet]. 2006 Mar [cited 2022 May 25];2(3). Available from: https://www.ncbi.nlm.nih.gov/pmc/articles/PMC1409813/

16. Staley K. Molecular mechanisms of epilepsy. Nat Neurosci. 2015 Mar;18(3):367–72.

17. Lu T, Trussell LO. Inhibitory Transmission Mediated by Asynchronous Transmitter Release. Neuron. 2000 Jun 1;26(3):683–94.

18. Hjelmstad GO. Interactions Between Asynchronous Release and Short-Term Plasticity in the Nucleus Accumbens Slice. J Neurophysiol. 2006 Mar;95(3):2020–3.

19. Pintaudi M, Calevo MG, Vignoli A, Parodi E, Aiello F, Baglietto MG, et al. Epilepsy in Rett syndrome: Clinical and genetic features. Epilepsy Behav. 2010;19(3):296–300.

20. Corrigan BW, Gulli RA, Doucet G, Roussy M, Luna R, Pradeepan KS, et al. Distinct neural codes in primate hippocampus and lateral prefrontal cortex during associative learning in virtual environments. Neuron. 2022 Jul 6;110(13):2155-2169.e4.

21. Spike Sorting Protocol | Axion Biosystems [Internet]. [cited 2023 Jun 21]. Available from: https://www.axionbiosystems.com/resources/culture-protocol/spike-sorting-protocol

22. Shimazaki H, Shinomoto S. Kernel bandwidth optimization in spike rate estimation. J Comput Neurosci. 2010;29(1):171–82.